ChemComm

COMMUNICATION

View Article Online
View Journal | View Issue

Cite this: *Chem. Commun.*, 2024, **60**, 14589

Received 24th August 2024,
Accepted 28th October 2024

DOI: 10.1039/d4cc04331f

rsc.li/chemcomm

Interphase formation *versus* fluoride-ion insertion in tunnel-structured transition metal antimonites†

Alice R. Giem,[ab] Jaime R. Ayala,[ab] Jingxiang Cheng,[ab] Conan Weiland,[c] Cherno Jaye,[c] Daniel A. Fischer[c] and Sarbajit Banerjee *[ab]

Fluoridating reagents are used to model interfacial reactions in fluoride-ion batteries. Topochemical F-ion insertion is seen for one-dimensional (1D) tunnel-structured $FeSb_2O_4$ but interphase formation comprising antimony (oxy)fluorides is observed for $MnSb_2O_4$.

Grid-level energy storage requires a diversity of battery chemistries so as to alleviate stresses on current mineral supply chains and to provide safer alternatives to Li-ion batteries.[1–3] "Beyond Li" alternatives such as Na-ion batteries are yet to realize comparable energy densities, and often do little to diversify materials palettes.[4,5] Fluoride-ion batteries, which implement fluoride anions as charge carriers have received considerable attention as an orthogonal alternative with the potential to alleviate supply chain challenges and preclude the need for metal electrodeposition.[6–10] Fluoride conversion electrodes have shown promise but challenges remain with regards to high temperatures for successful operation, large volume changes, and sluggish fluoride-ion diffusion.[6–8] Much recent attention has focused on the design of insertion-based fluoride electrode materials where the integrity of the structural framework of insertion electrodes is preserved upon F-ion insertion/deinsertion.[11] However, a key consideration is the competition between ion insertion and interphase formation.[12] Here, we use fluoridating reagents, XeF_2 and $NOBF_4$, as models for interfacial electrode reactions to contrast F-ion reactivity in 1D tunnel-structured $FeSb_2O_4$ and $MnSb_2O_4$, which both adopt the schafarzikite-type structure but with distinctive oxidation potentials (0.771 and 1.56 *vs.* standard hydrogen electrode (SHE) for Fe^{2+}/Fe^{3+} and Mn^{2+}/Mn^{3+}, respectively).[13] We utilize a broad suite of spectroscopic methods to probe chemical reactivity in model F-ion insertion hosts to differentiate between interphase formation and insertion reactions.

The schafarzikite-type MA_2O_4 structure sketched in Fig. 1 (M = transition metal, A = p-block element with stereochemically active lone pairs) forms 1D tunnels defined by corner-shared

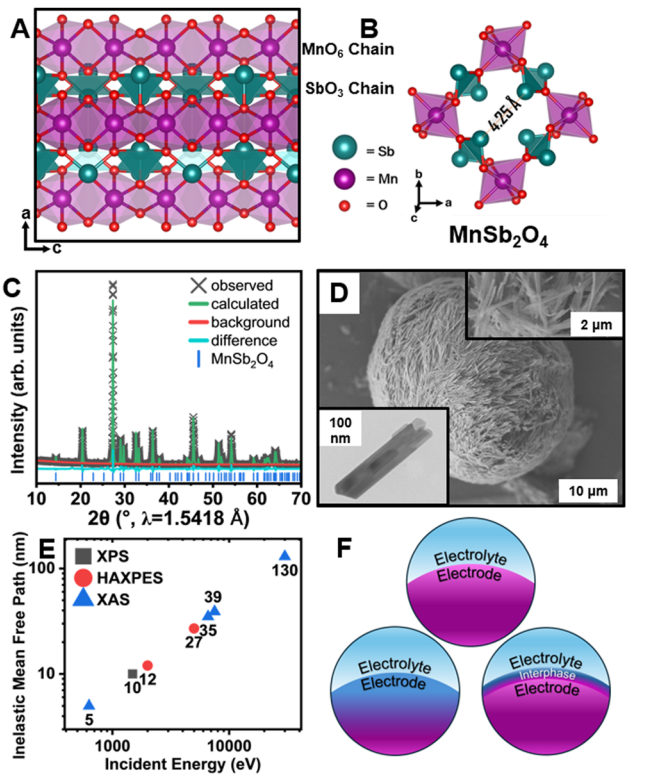

Fig. 1 Structure and characterization of $MnSb_2O_4$. (A) Schafarzikite-type $MnSb_2O_4$ viewed along (010); (B) 1D tunnel of $MnSb_2O_4$ viewed along the c direction. (C) Rietveld-refinement to powder XRD pattern used to obtain the structures in (A) and (B). (D) SEM image of $MnSb_2O_4$ nanorods; top inset shows magnified SEM; bottom inset shows a TEM image. (E) IMFP of an electron calculated based upon the incident energy for XPS, HAXPES, and XAS measurements. (F) Schematic illustration of F-ion reactivity.

[a] *Department of Chemistry, Texas A&M University, College Station, TX, 77843, USA. E-mail: banerjee@chem.tamu.edu*
[b] *Department of Material Science & Engineering, Texas A&M University, College Station, TX 77843, USA*
[c] *Material Measurement Laboratory, National Institute of Standards and Technology, Gaithersburg, MD 20899, USA*

† Electronic supplementary information (ESI) available. See DOI: https://doi.org/10.1039/d4cc04331f

$[MO_6]$ octahedra and $[AO_4]$ tetrahedra.[14–16] The stereochemical activity of $5s^2$ electron lone pairs of Sb^{3+} cations defines a large one-dimensional tunnel with an abundance of interstitial sites that can accommodate F-ions (Fig. 1B). In $FeSb_2O_4$, electron lone pair repulsions mediate frustrated coordination and ensure low site-to-site diffusion barriers whilst redox compensation is engendered through formal oxidation of Fe centers upon F-ion insertion.[14] The greater oxidation potential of the d-block cation in $MnSb_2O_4$ holds promise for accessing a higher voltage but the more challenging redox also renders parasitic reactions more probable.[17] While reversible room-temperature F-ion insertion with stoichiometries up to $x \approx 1$ can be accessed for $FeSb_2O_4F_x$,[14,15] complex interphasic products are instead stabilized upon reaction with $MnSb_2O_4$.

Interphase formation at oxide surfaces has attracted much recent attention given the critical role of interphasic products in mediating ion transport, surface stresses, and preservation of electrolyte/electrode connectivity.[18,19] Little is known about interphase formation in anion batteries. Here, we use diverse X-ray absorption and emission spectroscopy probes of varying penetration depth (Fig. 1E) to examine interphase formation in $MnSb_2O_4$ (Fig. 1F).

$MnSb_2O_4$ powders were obtained through a hydrothermal synthesis as described in the ESI.† A powder X-ray diffraction (XRD) pattern and Rietveld refinement is shown in Fig. 1C (see also Table S1, ESI†).[20] $MnSb_2O_4$ is isostructural to $FeSb_2O_4$ and crystallized in the tetragonal $P4_2/mbc$ space group. $MnSb_2O_4$ affords a larger tunnel width of 4.25 Å (Fig. 1B) as compared to 4.14 Å for $FeSb_2O_4$.[21,22] The obtained powders adopt a single-crystalline needle-like morphology (Fig. 1D and Fig. S1, ESI†).

Fluoridation reactions were initially performed using XeF_2 in acetonitrile under a diverse range of conditions as described in the Methods section.[17] Under these conditions, $FeSb_2O_4$ can be fluoridated to insert unitary fluoride ions per Fe center.[14,15] Powder XRD measurements and results from Rietveld refinement for fluoridation of $MnSb_2O_4$ are shown in Fig. S2 and Table S2 (ESI†). Scanning electron microscopy (SEM) and energy-dispersive X-ray spectroscopy (EDS) characterization is shown in Fig. S3 with Fig. S4 (ESI†) showing transmission electron microscopy (TEM) imaging including lattice resolved high-resolution TEM and selected area electron diffraction (SAED). Minimal changes of lattice parameters are observed in powder X-ray diffraction even though EDS elemental maps demonstrate some reactivity and remanence of fluorine-containing species. Definitive identification of the reaction products is enabled by synchrotron X-ray spectroscopy measurements, which provide a means of distinguishing insertion and interphase formation (Fig. 1F).

X-ray absorption near-edge structure (XANES) spectroscopy measurements of the as-prepared and fluoridated $MnSb_2O_4$ are shown in Fig. 2. Soft X-ray (surface sensitive) Mn L-edge ($2p$–$3d$) spectra for XeF_2-treated $MnSb_2O_4$ are plotted in Fig. 2A. Corresponding Fe L-edge data for XeF_2-reacted $FeSb_2O_4$ are plotted in Fig. 2B. In contrast to $FeSb_2O_4$, where F-ion insertion brings about oxidation of the Fe center,[14,15] the Mn L_3-edge spectra with a pronounced absorption at 640 eV characteristic of divalent Mn do not evidence signatures of Mn oxidation upon treatment with XeF_2.[23] As such, both powder XRD and Mn L-edge XANES measurements do not support the notion of F-ion insertion. However, Fig. 2C shows that reaction of $MnSb_2O_4$ results in the emergence of the F K-edge ($1s$–$2p$), characteristic of fluoride moieties at the surface. This and the EDS measurements

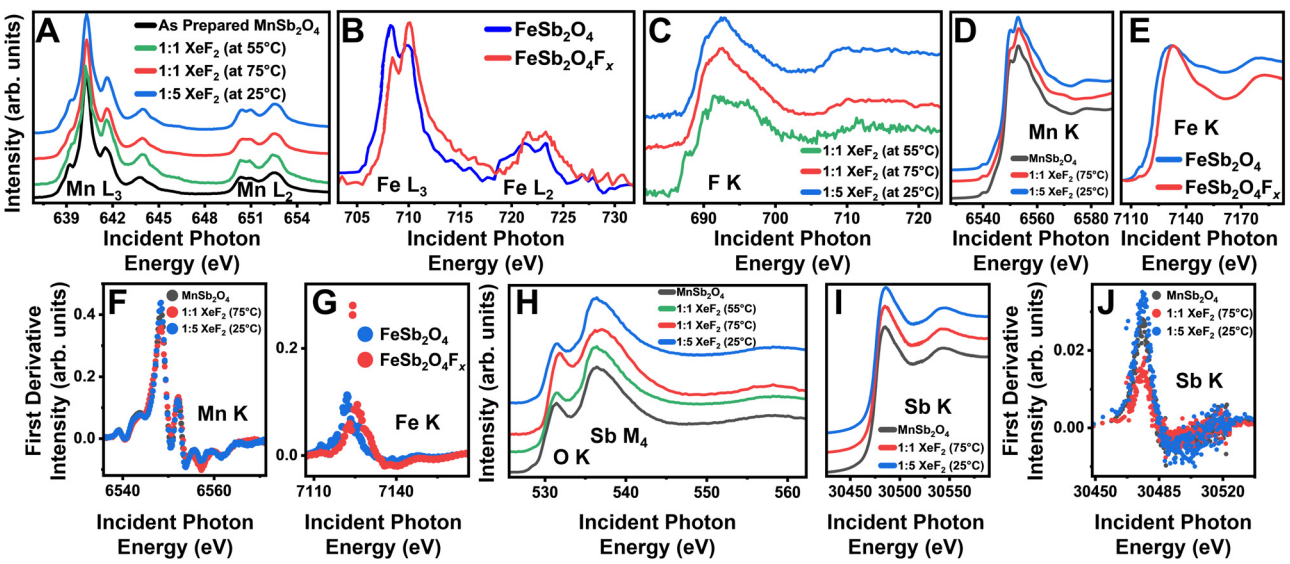

Fig. 2 XANES characterization of fluoridated products. XANES spectra collected for the as-prepared $MnSb_2O_4$ (black) and fluoridated products (green 1 : 1 molar ratio of XeF_2/CH_3CN at 55 °C, red 1 : 1 molar ratio of XeF_2/CH_3CN at 75 °C, and blue 1 : 5 molar ratio of XeF_2 in CH_3CN at 25 °C) at the (A) Mn L_3-/L_2-edges, (B) Fe L_3/L_2-edges, (C) F K-edge, (D) Mn K-edge, and (E) Fe K-edge. Additional spectra in (F) represent the first derivative of the Mn K-edge spectra, (G) first derivative of the Fe K-edge spectra, (H) Sb M_4-, O K-edges, first derivative of the Mn K-edge spectra, (I) Sb K-edge, and (J) first derivative of the Sb K-edge spectra. Panels (B), (E), and (G) are adapted with permission from Zaheer *et al.*[14] Copyright (2020) ACS Energy Lett.

in Fig. S2 (ESI†) suggest that fluorine is incorporated at least on particle surfaces through alternative reaction pathways.

Hard X-ray ("bulk"-sensitive) XANES measurements have been collected for Mn, Sb, and Fe at their corresponding K-edges (1*s*–2*p*). Contrasting Fig. 2D and E respectively, the Mn and Fe K-edges measured for XeF_2-reacted $MnSb_2O_4$ and $FeSb_2O_4$ show pronounced differences. The Fe K-edge spectrum shows a pronounced shift of *ca.* 3 eV of the white-line absorption, indicating bulk oxidation concomitant with F-ion insertion.[14,15] In contrast, only a subtle change in the shape of the Mn K-edge is observed (a *ca.* 5 eV shift is anticipated for the oxidation of Mn^{2+} to Mn^{3+}).[24] The differential spectrum in Fig. 2F further does not show significant changes again arguing against bulk F-ion insertion in $MnSb_2O_4$ (contrast to Fig. 2G for $FeSb_2O_4$).

To examine the fluoride product evidenced from Fig. 2C and Fig. S2 (ESI†), we next explore surface and bulk probes of Sb bonding. Surface-sensitive Sb M_4-edge (3*d*–4*f*) XANES spectra in Fig. 2H show modified relative intensities of pre-edge and white line absorption features at 531 eV and 536 eV, respectively. Subtle shifts of the absorption features indicate a change in the coordination environment of Sb whilst preserving a nominally trivalent antimony species. Sb K-edge (1*s*–2*p*) spectra in Fig. 2I do not show a pronounced shift of the white-line absorption; the differential spectra of the Sb K-edge plotted in Fig. 2J show an increase in the intensity of the peak at 30 475 eV. The modification of the Sb local structure is more evident in surface-sensitive Sb M_4-edge XANES as compared to the Sb K-edge, which probes deeper into the sample. As such, the XANES results suggest the stabilization of amorphous interphasic products that are predominantly a mixture of fluorides and oxyfluorides of trivalent antimony.[25]

We next probe XeF_2-reacted $MnSb_2O_4$ using hard X-ray photoemission spectroscopy (HAXPES).[26] The Mn 2p core level of the as-prepared $MnSb_2O_4$ is shown in Fig. 3A. The satellite peak at 650 eV binding energy is a distinct feature of Mn^{2+}.[27] Fig. 3B and C contrast the Mn 2p core levels of $MnSb_2O_4$ after XeF_2 treatment. Integrating the satellite peaks corroborates that the Mn centers do not undergo bulk oxidation as would be expected upon F-ion insertion. Fig. 3D shows the emergence of remnant F-containing species upon XeF_2 treatment. Fig. 3E depicts the Sb 3d core level with the Sb $3d_{3/2}$ centred at approximately 540 eV, verifying the preservation of the Sb^{3+} formal oxidation state. The Sb $3d_{5/2}$ core level feature overlaps with the O 1s core level. The decrease in area observed in the Sb $3d_{5/2}$/O 1s peak indicates a less oxygen rich surface upon 1 : 3 XeF_2 treatment (Fig. 3E), suggesting accumulation of fluoride/oxyfluoride interphasic products.

To probe the electronic structure of $MnSb_2O_4$ before and after XeF_2 treatment, valence band (VB) spectra were acquired using energy-variant HAXPES (Fig. 3E and F). The photoionization cross-sections of orbitals have an incident energy-dependent decay that can be utilized to decipher orbital contributions.[14,22] Orbital subshells with higher orbital angular momentum (*e.g.*, d and f shells) contribute greater intensity to the VB spectrum at lower incident energies. In contrast, at higher energies, the s and p shells make a greater contribution to the VB.[14] A subtle diminution in intensity is visible for fluoridated $MnSb_2O_4$ at

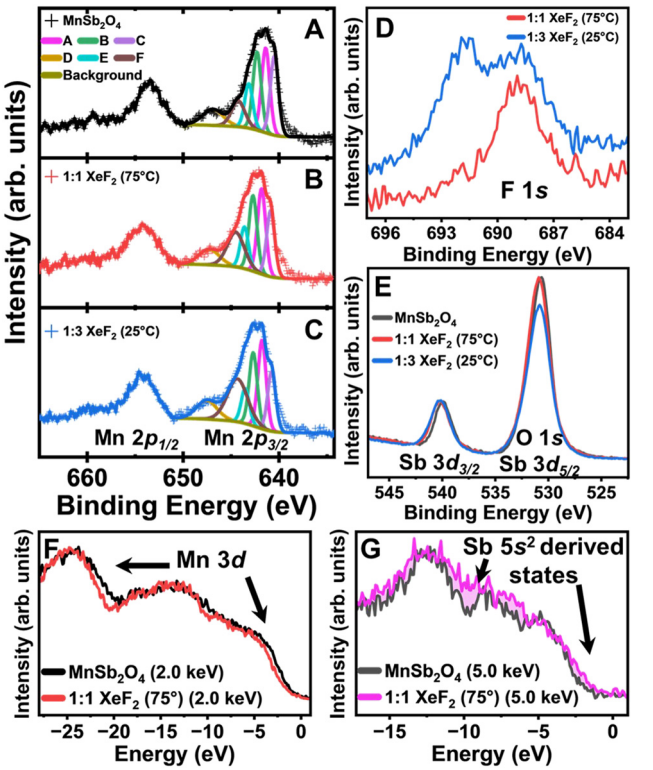

Fig. 3 HAXPES spectra of $MnSb_2O_4$ and derivatives collected at 2 keV incident energy unless otherwise stated; (A) Mn 2p core level of the as-prepared $MnSb_2O_4$ shown with fits (A)–(F) for Mn $2p_{3/2}$; (B) Mn 2p core level after a 1 mol treatment with XeF_2 in CH_3CN; (C) Mn 2p core level after a 3 mol excess treatment with XeF_2; (D) F 1s core level spectra after XeF_2 treatments; (E) Sb 3d core level. VB spectra of $MnSb_2O_4$ before and after the reaction with 1 mol XeF_2 collected at an incident energy of (F) 2 keV and (G) 5 keV.

2 keV incident energy indicating less Mn 3d character upon fluoridation. At 5 keV incident energy (Fig. 3G), an increase in the states near the Fermi level suggests greater contributions from the Sb lone-pair states hybridized with F 2p states upon fluoridation. These observations are furthermore consistent with the accumulation of an Sb-rich (and Mn-poor) interphasic product. While increasing temperature accelerates F-ion insertion in $FeSb_2O_4$,[16] the reactivity of $MnSb_2O_4$ and the speciation of the interphasic product is not substantially modified from room temperature as consistent with a surface passivation reaction.

Fig. S5 (ESI†) shows density of states (DOS) calculations for $MnSb_2O_4$ and $FeSb_2O_4$. Atom-projected partial DOS plots illustrate that Fe 3d–O 2p states are located at the valence band edge and above Sb-derived states. In contrast, Mn 3d–O 2p states are strongly overlapped with Sb states at the valence band edge of $MnSb_2O_4$. As such, Fe and Sb are preferentially oxidized by the fluoridating reagents in $FeSb_2O_4$ and $MnSb_2O_4$, respectively. Fig. S6 (ESI†) shows that F-ion insertion to form a putative $MnSb_2O_4F_x$ is unlikely because of strong distortions needed to push Mn states above Sb states.

The most significant change in HAXPES spectra is observed in the F 1s region (Fig. 3D). Treatment with a 1 : 1 molar ratio of XeF_2 yields a singular F 1s feature, but upon treatment with a 3-molar excess of XeF_2, a second F 1s feature is observed. The

features can be ascribed to a combination of surface insertion and interphase formation or fluoride/oxyfluoride interphases. An alternative fluoridation agent, $NOBF_4$, has furthermore been examined because of its high oxidizing power.[28] $NOBF_4$ has an oxidation potential of 1.7 V *vs.* SHE, which is greater than the oxidation potential of Mn by 0.14 V. Fig. S7 (ESI†) shows a powder XRD pattern acquired for $MnSb_2O_4$ after reaction with $NOBF_4$ in acetonitrile. The reaction does not bring about an evident change of lattice parameters (Table S3, ESI†). SEM-EDS in Fig. S8 (ESI†) provides confirmation of fluoride incorporation with Fig. S9 (ESI†) showing TEM, including lattice-resolved high-resolution TEM and SAED.

Fig. S10 (ESI†) plots a Mn L_3-edge XANES spectrum acquired for $MnSb_2O_4$ after treatment with $NOBF_4$. The spectrum shows a slight shift of the white line absorption and diminution of the pre-edge feature at 639 eV. Fig. S11 (ESI†) shows Sb M_4-edge and O K-edge XANES spectra for the as-prepared $MnSb_2O_4$ and after treatment with a 3-molar excess of $NOBF_4$. Similar to Fig. 2B, no shift of the white line absorption energy is observed, which indicates retention of a nominally trivalent oxidation state for Sb. However, a pronounced modification of relative intensities of features centred at 531 eV and 536 eV is suggestive of a change in the Sb local coordination environment. F K-edge XANES spectra in Fig. S11B (ESI†) indicate the presence of anionic fluoride species after $NOBF_4$ treatment. Core-level HAXPES spectra (Fig. S11B–D, ESI†) show pronounced changes suggestive of the accumulation of an interphasic product. The O 1s core level is significantly decreased in intensity as compared to overlapping Sb 3d states, indicating that there is less oxygen on the surface (Fig. S11C, ESI†). The shift in binding energy for the Sb $3d_{3/2}$ core level further suggests an alteration of the surficial Sb local coordination environment. Based on these observations, the interphase layer is most-likely formed by amorphous antimony fluorides and oxyfluorides, such as SbF_3 or a F-rich oxyfluoride such as $Sb_3O_2F_5$ (Fig. S11E–G, ESI†). Table S4 (ESI†) provides balanced chemical equations for the formation of each of these species. While $NOBF_4$ is a stronger oxidizing reagent, based on the electronic structure considerations depicted in Fig. S5 (ESI†), it promotes increased antimony oxidation and exacerbates the formation of the interphasic product. Fig. S12 (ESI†) depicts crystal structures of the candidate materials but based on X-ray scattering, the interphasic products do not appear to have long-range order.

Understanding the competitive nature of insertion *versus* interphase formation is key to the design and discovery of insertion electrodes of fluoride-ion batteries. We find a sharp contrast between low-dimensional $FeSb_2O_4$ and $MnSb_2O_4$, both of which crystallize in a schafarzikite-type structure with a 1D tunnel. While the former reversibly accommodates F-ions in interstitial sites along its tunnel, the latter is characterized by very limited bulk F-insertion. The insertion of fluoride-ions is instead constrained by the formation of an interphase layer on the surfaces of the $MnSb_2O_4$ particles. While Mn affords a higher oxidation potential, the overlap of Mn 3d-derived states with Sb states at the valence band edge promotes the preferential formation of amorphous antimony fluoride or antimony oxyfluoride interphasic products. Understanding the reactivity of model systems will assist in the future realization of viable F-ion insertion electrodes and full batteries.

The authors acknowledge support from the Welch Foundation under award A-1978-20190330. This research used resources of the National Synchrotron Light Source II under Contract DE-SC0012704.

Data availability

The data supporting this article have been included as part of the ESI.†

Conflicts of interest

The authors have no conflicts of interest to declare.

Notes and references

1 A. Zeng, *et al.*, *Nat. Commun.*, 2022, **13**, 1341.
2 C. Xu, *et al.*, *Commun. Mater.*, 2020, **1**, 1–10.
3 P. Xu, *et al.*, *Trends Chem.*, 2021, **3**, 620–630.
4 B. Esser, *et al.*, *Adv. Energy Mater.*, 2024, 2402824.
5 H. S. Hirsh, *et al.*, *Adv. Energy Mater.*, 2020, **10**, 2001274.
6 M. A. Reddy and M. Fichtner, *J. Mater. Chem.*, 2011, **21**, 17059–17062.
7 A. W. Xiao, *et al.*, *Joule*, 2021, **5**, 2823–2844.
8 V. K. Davis, *et al.*, *Science*, 2018, **362**, 1144–1148.
9 D. McTaggart, *et al.*, *ChemSusChem*, 2023, **16**, e202300486.
10 V. Vanita, *et al.*, *J. Mater. Chem. A*, 2024, **12**, 8769–8784.
11 M. A. Nowroozi, *et al.*, *J. Mater. Chem. A*, 2018, **6**, 4658–4669.
12 J. L. Andrews, *et al.*, *ACS Energy Lett.*, 2022, **7**, 2340–2348.
13 S. G. Bratsch, *J. Phys. Chem. Ref. Data*, 1989, **18**, 1–21.
14 W. Zaheer, *et al.*, *Cell Rep. Phys. Sci.*, 2021, **2**, 100592.
15 W. Zaheer, *et al.*, *ACS Energy Lett.*, 2020, **5**, 2520–2526.
16 B. P. de Laune, *et al.*, *Inorg. Chem.*, 2017, **56**, 10078–10089.
17 C. K. Blakely, *et al.*, *J. Solid State Chem.*, 2020, **289**, 121490.
18 W. Li, *et al.*, *Nat. Commun.*, 2017, **8**, 14589.
19 C. D. Quilty, *et al.*, *Chem. Rev.*, 2023, **123**, 1327–1363.
20 M. Roelsgaard, *et al.*, *Dalton Trans.*, 2016, **45**, 18994–19001.
21 K. Tolborg, *et al.*, *IUCrJ*, 2020, **7**, 480–489.
22 J. V. Handy, *et al.*, *Chem. Mater.*, 2022, **34**, 1439–1458.
23 B. Gilbert, *et al.*, *J. Phys. Chem. A*, 2003, **107**, 2839–2847.
24 T. S. Wu, *et al.*, *Appl. Phys. Lett.*, 2012, **101**, 022408.
25 S. Imran Ali and M. Johnsson, *Dalton Trans.*, 2016, **45**, 12167–12173.
26 Z. W. Lebens-Higgins, *et al.*, *J. Phys. Chem. Lett.*, 2020, **11**, 2106–2112.
27 E. S. Ilton, *et al.*, *Appl. Surf. Sci.*, 2016, **366**, 475–485.
28 A. R. Wizansky, *et al.*, *J. Solid State Chem.*, 1989, **81**, 203–207.

